Piercing a liquid surface with an elastic rod: buckling under capillary forces

Sébastien Neukirch[*], Benoît Roman[†], Benoît de Gaudemaris[†], and José Bico[†]

[*]Laboratoire de modélisation en mécanique (UMR 7607: CNRS, Université Paris VI)
[†]Physique et Mécanique des Milieux Hétérogènes (UMR 7636: CNRS, ESPCI, Paris VI, Paris VII)
Paris, France.

November 3, 2006

Abstract

When a thin elastic structure comes in contact with a liquid interface, capillary forces can be large enough to induce elastic deformations. This effect becomes particularly relevant at small scales where capillary forces are predominant, for example in microsystems (Micro-Electro-Mechanical Systems or microfluidic devices) under humid environments. In order to explore the interaction between capillarity and elasticity, we have developed a macroscopic model system in which an initially immersed vertical elastic rod is raised through a horizontal liquid surface. We follow a combined approach of experiments, theory and numerical simulations to study this system. In spite of its apparent simplicity, our experiment reveals a complex phase diagram, involving large hysteretic behaviour. We employ Kirchhoff equations for thin elastic rods and use path-following methods from which we obtain a variety of equilibrium states and associated transitions that are in excellent qualitative and quantitative agreement with those observed experimentally.

1   Introduction

Capillary forces are responsible for a large range of everyday observations; for example the shape of rain droplets, the imbibition of a sponge [7], the clumping of wet hair into bundles [2]. They also allow aquatic insects to stand on water [12]. Although they are often negligible on macroscopic structures, surface capillary forces may be strong enough to deform compliant structures at small scales. From a more technological point of view, capillary-induced sticking can prevent the actuation of micro-cantilevers, mobile elements of Micro-Electro-Mechanical Systems (MEMS) [17, 19] or bio-mimetic materials [9]. Typical micro-fabrication processes often involve mask controlled reticulation in a liquid phase. The evaporation of the excess liquid generates menisci which sometimes cause the structures to collapse [21, 13] or to stick to the substrate [20]. Similar phenomena have recently been observed with carbon nanotube "carpets": upon the evaporation of a solvent, vertically aligned nanotubes self-assemble into conical "teepee" structures [16] and can produce intriguing cellular patterns [3]. Besides engineering processes, capillary forces also have important consequences in biology such as the buckling of the airway lumen induced by surface tension which can eventually cause the lethal closure of lung airways (known as neonatal Respiratory Distress Syndrome) [10, 11].

In the present paper we study the equilibrium states of a single elastic rod raised through the surface of a wetting liquid, a paradigm for a novel type of fluid-structure interaction where surface tension becomes more important than inertial or viscous forces. The related situation of a rod in a spherical bubble, where

1

it may either pierce or conform to the surface, has been previously investigated theoretically in connection with various biological systems [5]. Here, we develop an idealised model experimental system built at the macroscopic scale for the case of a flat interface and investigate in detail the possible equilibrium states as well as their dynamics. We show that our system exhibits a surprisingly complex phase diagram. The experimental study is complemented by a theoretical analysis using Kirchhoff's equations for thin elastic rods [1] coupled with capillary, pressure, and gravity forces [15]. Numerical integration of the derived equations and continuation of their solutions shows an excellent quantitative and qualitative agreement with our experimental observations, thereby validating our model of interaction between capillary forces and flexible structures and shedding light on the associated mechanical instabilities.

This paper is organised as follows. In section 2 we first describe the experimental setup and present typical observations. We give in section 3 a brief introduction to capillary forces and define the *elasto-capillary length* over which elasticity and capillarity effects are comparable. Then, in section section 4 we show theoretically and experimentally that a long enough rod can buckle when submitted to surface tension forces. We follow with a comprehensive theoretical description of the bent states (section 5). We also display the phase diagram obtained by numerical integration of our model, where the transitions between the different configurations are represented. In section 6 we confront this phase diagram to experiments, and finally study some peculiar properties of the bent shapes.
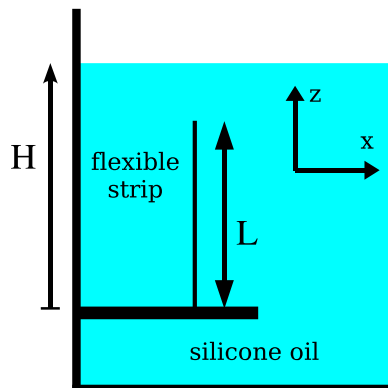
2 Experimental setup

Figure 1: Experimental setup : an elastic strip or a fibre is clamped at its base on a horizontal rigid support. We lower/raise the support along a pole so that the strip gradually emerges from the bath of silicone oil.

A flexible strip (polyester, thickness $e = 25$ and 50μm, width $w = 20$ mm, density 1.4, bending rigidity $EI = 1.24 \times 10^{-7}$ and 1.5×10^{-6} J·m) is clamped on a horizontal support which can be displaced vertically. We also used glass fibres ($EI = 6.4 \times 10^{-9}$J·m) with circular cross-section (radius $R = 18\mu$m). The bending rigidity EI was measured from a classical sagging cantilever experiment. The apparatus is initially immersed in a bath of silicon oil (viscosity $\sim 2 \times 10^{-2}$ Pa·s and surface tension $\gamma = 20.6 \times 10^{-3}$ N/m) and is progressively raised up toward the liquid interface. Our control parameters are thus the bath height H, which is defined as the distance (possibility negative) between the base of the strip and the liquid surface, and the length of the strip L, which we changed in different experiments. We chose

silicon oil because it perfectly wets polyester, preventing any hysteresis in its wetting properties (the wetting contact angle is always zero).

The system nevertheless exhibits a strong hysteretical behaviour, as shown in figure 2 which illustrates a typical experiment with a relatively long strip. In A, the strip is initially totally immersed, and the fluid level is quasistatically lowered. When the tip comes in contact with the liquid surface, the strip does not pierce the interface, but instead buckles, and bends gradually as the bath height is reduced (B-C). In D, the strip finally pierces the interface, but both ends remain immersed while its middle part arches out of the liquid bath. The free end finally detaches from the bath (E to F) and the strip recovers its original straight shape. Starting from state F, the experiment is then conducted backward, i.e. the strip is progressively immersed. The sequence of equilibrium states is different: the strip remains straight with its clamped base immersed (G). But when the bath height is large enough it suddenly bends and returns to the equilibrium observed at the beginning of the withdrawal (state B). Other scenarios are possible: in particular a short strip can pierce the surface without being deflected and the experiment is then reversible.
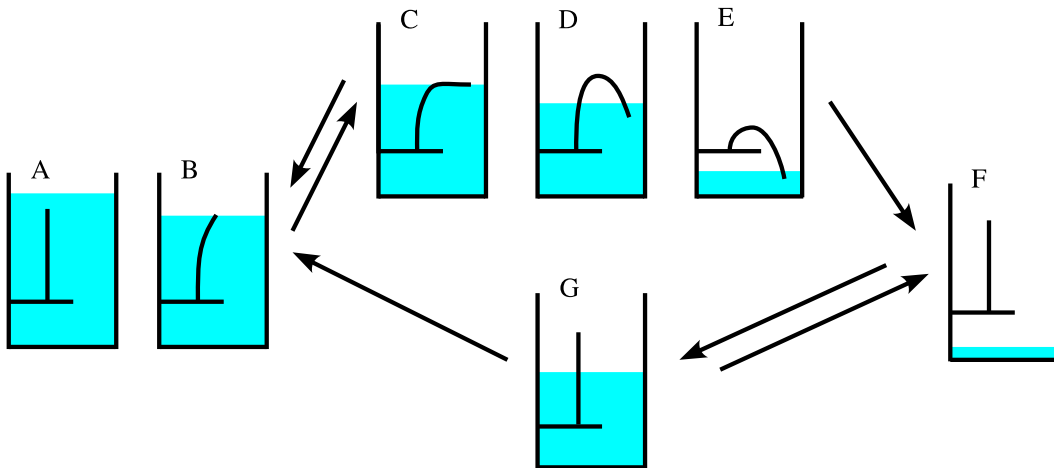

Figure 2: Sequence of experimental equilibrium states of a long strip, when lowering then increasing the bath height.

3 Capillary buckling

In this section we give a short introduction to capillary forces, and show that the two transitions where the straight equilibrium loses its stability (fig.2: A to B during withdrawal, and G to B during immersion) are in fact buckling transitions induced by capillary forces.

3.1 Capillary forces

Creating an interface between two phases α and β requires that molecular $\alpha - \alpha$ and $\beta - \beta$ bonds be broken and replaced by $\alpha - \beta$ bonds. The contrast in molecular affinities results into an energy cost $\gamma_{\alpha\beta}$ per unit area of the created interface [7]. Equivalently, γ can be seen as a surface tension. When three phases (e.g. liquid, gas, and solid) are involved, they meet along a contact line and one should consider

tension forces for each of the three phases. As a result, when a solid touches an interface, capillary forces are generated at the contact line. In the perfectly wetting conditions we consider here, the liquid surface is tangent to the solid along the contact line (except at edges, where the tangent is not defined). In addition, since a precursor liquid film entirely coats the solid surface, one only has to consider the surface tension γ between liquid and air [6]. From a mechanical point of view, the capillary force acting on a solid corresponds to a distributed force with strength γ per unit length (in our case, $\gamma = 20.6$ mN/m), oriented along the tangent of the liquid surface.
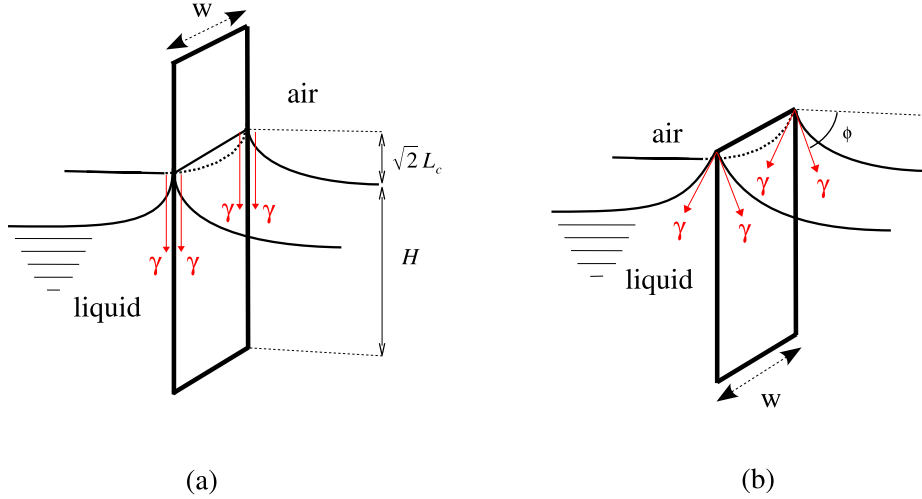

Figure 3: Elastic strip piercing (a) or only deflecting (b) a liquid surface. The (vertical) force provided by the liquid surface depends on the meniscus height.

As an illustration, we show in fig.3(a) a rigid vertical strip emerging through a horizontal fluid surface, with height H. Since the liquid perfectly wets the solid, the tangent of the liquid surface is vertical at the contact line. The surface is then deformed into a meniscus whose extension is limited by gravity that tends to keep the surface horizontal. Deforming an interface also generates a pressure discontinuity (Laplace pressure) $\Delta P = \gamma/R$, where R^{-1} is the surface curvature [7]. The actual shape of the meniscus results from a balance between the Laplace pressure and the hydrostatic pressure $\Delta P = \rho g(Z - H)$, where $Z - H$ is the local height of the meniscus:

$$\rho g(Z - H) = \gamma/R. \tag{1}$$

In this geometry, the surface curvature is just $R^{-1} = d\phi/ds$, where s is the arc-length along the surface, and ϕ the angle between its tangent and the horizontal (i.e. $dZ/ds = \sin\phi$), see fig.3. Using (1) and integrating yields:

$$(Z - H)^2 = 2L_c^2(1 - \cos\phi), \tag{2}$$

where $L_c \overset{\text{def}}{=} \sqrt{\gamma/(\rho g)}$ is the *capillary length* (1.5 mm for silicon oil) [4]. The maximal height at the contact point is $\sqrt{2}\,L_c$ when $\phi = \pi/2$. The total fluid force acting on the solid is the sum of the integrated hydrostatic pressure and surface tension forces. In our case, pressure forces compensate at each point, and the total force scales with the perimeter:

$$F_{cross} = 2\gamma w, \tag{3}$$
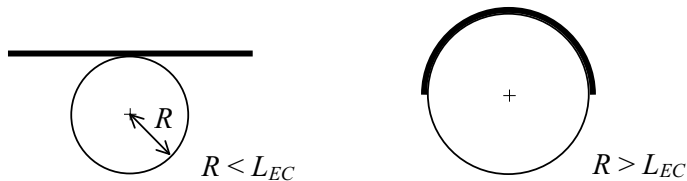
4

R

$R < L_{EC}$

$R > L_{EC}$

Figure 4: An elastic strip is brought in contact with a wet cylinder (a): if the radius of the cylinder is larger than the elastocapillary length L_{EC}, the strip spontaneously wraps the cylinder (b)

where the thickness e of the strip is neglected in the computation of the perimeter.

If the height of the rigid strip does not exceed $H + \sqrt{2}\,L_c$, the strip does not pierce but only deforms the interface, fig.3(b). Since the meniscus meets the strip at a sharp edge, it is not (apparently) tangent to the solid at the contact line (the tangency is restored at a small scales, where the corner appears round). Consequently the angle ϕ takes any value between 0 and $\pi/2$. In this case the restoring force remains vertical because of left/right symmetry, and reads $F = 2w\gamma \sin \phi < F_{cross}$.

To summarise, we see that when a vertical rigid strip is brought up to a horizontal liquid interface, it progressively deforms it, and only pierces it when the vertical deflection reaches $\sqrt{2}\,L_c$. The applied force is then F_{cross}. Since L_c is rather small compared to the other lengths in the problem, we will always first consider a description at zero capillary length where the height of the meniscus is neglected. Thus the interface can be regarded as rigid and planar, capable of exerting a vertical force with a maximal value $2\gamma w$ on a vertical strip.

3.2 Elasto-capillary length

What is the magnitude of the effect of capillary forces on an elastic structure? Consider for example an elastic strip of length L put in contact with a wet rigid cylinder of radius R. The strip can either remain straight without any change of energy (fig.4a), or adhere to the cylinder with a gain of surface energy but with a loss of bending energy (fig.4b). The surface energy is reduced by $2\gamma wL$ if the strip adheres to the cylinder, but at the cost of a bending energy $EIL/(2R^2)$, if w is the width, E the Young's modulus and I the second moment of area of the section of the elastic body. It follows that the strip spontaneously wraps and sticks to the cylinder as long as the cylinder diameter is larger than the *elasto-capillary length*:

$$L_{EC} \overset{\text{def}}{=} \sqrt{\frac{EI}{\gamma w}}.$$

$$(4)$$

This particular example illustrates the fact that L_{EC} gives the order of magnitude of the radius of curvature generated by surface tension forces. Equivalently, a structure with length comparable or greater than $L_{EC}/2$ will be severely deflected by a liquid surface. In our experiments the strips are chosen to be fairly flexible, so that L_{EC} is of the order of few centimetres. Now if the scale of a given structure is divided by a factor α, the second moment of area I scales as α^{-4} which leads to $L_{EC} \sim \alpha^{-3/2}$. At the same time the length L decreases like $L \sim \alpha^{-1}$, so it eventually becomes larger than L_{EC}: at small enough scales, the effect of surface tension on thin elastic structures becomes dominant.

5

4 Buckling under capillary forces

Turning now to our problem, we consider an elastic beam clamped at its base and subjected to a concentrated vertical compressive load F at its other end. Classic elasticity theory tells us that such a straight beam becomes unstable and buckles when F is larger than the critical value:

$$F^\star \overset{\text{def}}{=} \left(\frac{\pi}{2}\right)^2 \frac{EI}{L^2},$$
(5)

where E is the Young's modulus, I the second moment of area of the beam section, and L the length of the beam.

This compression threshold $F^\star$, known as the Euler buckling load [1, 22], decreases with the length L of the beam. Equating F_{cross} to $F^\star$ yields the maximum length L_b above which a beam (of width w) buckles when compressed by surface tension :

$$L_b \overset{\text{def}}{=} \frac{\pi}{2} \sqrt{\frac{EI}{2\gamma w}} = \frac{\pi}{2\sqrt{2}} L_{EC}.$$
(6)

Note that this buckling length L_b is proportional to the characteristic elasto-capillary length defined above.
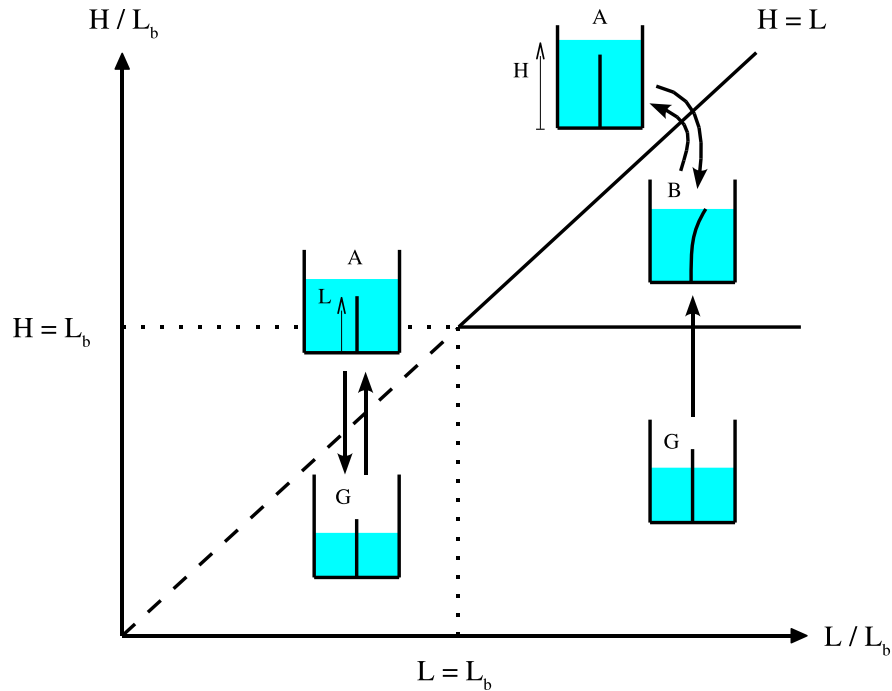

Figure 5: Parameter regimes for the buckling of a straight beam, of length L, by surface tension. Short beams ($L < L_b$) pierce the liquid interface whereas longer beams are deflected.

We now consider an elastic beam entirely immersed in a bath, and start lowering the bath height H. When the surface reaches the upper end of the beam ($H = L$), the interfacial force may (or may not) be

strong enough to deflect it: if $L < L_b$, the beam stays straight and pierces the surface (from A to G in fig.5), whereas if $L > L_b$ the beam buckles (transition from A to B in fig.5).

We now start with a completely withdrawn straight beam (case F in fig.2) and gradually increase the bath level. As long as the immersed part of the beam (which is equal to H) is lower than L_b, the beam remains straight. If the beam is long enough ($L > L_b$), the immersed length H eventually reaches L_b and the capillary force is large enough to bend the beam which snaps to a deflected state (transition from G to B in fig.5). Naturally, shorter beams ($L < L_b$) never buckle during immersion (from G to A in fig.5).

Additional transitions observed experimentally between the deflected states motivate a specific investigation of such states, which is developed in the next section.

5   The bent states

We present here the theoretical framework which we use to study the post-buckled equilibrium configurations. We focus on the elastic response of the beam, while the two-dimensional meniscus shape obeys eq.2.

5.1   Kirchhoff model of elastic rods in the planar case

We consider here a slender elastic object that has a length L much larger than its thickness e. As long as the curvature remains small (compared to $1/e$), the mechanical state of such a beam is accurately described by a 1D elastic theory: the stress fields in the material are averaged in each cross-section [1]. This yields two vectorial quantities: the internal moment $\boldsymbol{M}$ and the internal force $\boldsymbol{N}$ that only depend on the arc-length S along the beam. The equilibrium equations of this continuous elastic medium are (local) differential equations. If one considers an infinitesimal part of the beam (say in $[S; S + \delta S]$) the balance of the forces and the moments acting on it yield, respectively:

$$\boldsymbol{N}' + \boldsymbol{P} = \boldsymbol{0} \,, \tag{7}$$

$$\boldsymbol{M}' + \boldsymbol{R}' \times \boldsymbol{N} = \boldsymbol{0} \,, \tag{8}$$

where $' \equiv \frac{d}{dS}$, $\boldsymbol{R}(S) = (X, Y, Z)$ is the position of the centre line of the beam and $\boldsymbol{P}(S)$ accounts for external forces. These equilibrium equations for an elastic beam are referred to as the Kirchhoff equations. We choose to non-dimensionalise the physical quantities using the buckling length L_b defined in eq. (6). This yields dimensionless quantities: $\boldsymbol{n} \overset{\text{def}}{=} \frac{\boldsymbol{N} L_b{}^2}{EI}$, $\boldsymbol{m} \overset{\text{def}}{=} \frac{\boldsymbol{M} L_b}{EI}$, $\boldsymbol{r} \overset{\text{def}}{=} \frac{\boldsymbol{R}}{L_b}$, and $s \overset{\text{def}}{=} \frac{S}{L_b}$. The beam is also assumed to be unshearable and inextensible. We show in appendix B (section 10) that the boundary conditions we consider constrain the deflected configurations to lie in the (X, Z) plane and the beam to stay untwisted. Hence we are in the case of an Euler planar elastica, with the possibility of distributed forces (modelled by $\boldsymbol{P}$) acting at discrete points or along continuous parts of the beam. The angle between the vertical and the tangent of beam is noted $\theta(S)$. We use a linear constitutive relation between the curvature of the beam θ' and the bending moment M_y: $M_y = EI\theta'$. The Kirchhoff equations

become:

$$
\begin{aligned}
n_x' &= -p_x &(9)\\
n_z' &= -p_z &(10)\\
m_y' &= n_z \sin\theta - n_x \cos\theta &(11)\\
x' &= \sin\theta &(12)\\
z' &= \cos\theta &(13)\\
\theta' &= m_y\,, &(14)
\end{aligned}
$$

and $n_y \equiv 0$, $m_x \equiv 0$, $m_z \equiv 0$, $y \equiv 0$ $\forall s$. Due to the non-dimensionalisation, EI no longer appears in the equations (9-14). We start the integration ($s = 0$) at the foot of the beam, which is anchored to the support, yielding the boundary conditions:

$$
x(0) = 0 = z(0)\,, \ \theta(0) = 0\,, \tag{15}
$$

and we integrate up to the end of the beam $s = L/L_b$ where other boundary conditions have to be fulfilled.

The meniscus is present in any region where the beam comes near the liquid surface: either at the end of the beam or at the positions where the beam crosses the surface. Its size, of the order of the capillary length L_c, is much smaller than the length L of the beam or the critical length L_b. In most configurations, it is then possible to discard the meniscus region and invoke a localised force that represents the surface interaction with the beam. Nevertheless in some specific cases, we have also performed computations including the meniscus shape and the liquid weight (see section 5.4).

5.2 Lightly deflected state

A beam with a length exceeding the critical length ($L > L_b$) buckles when it comes in contact with the liquid interface (i.e. when the bath height H is lowered to $H < L$). The beam then adopts a bent shape with a point contact at the interface, but does not cross it. We here present a description neglecting the meniscus height.
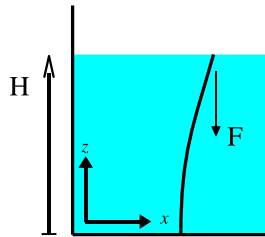

Figure 6: Lightly deflected state at null capillary length ($L_c = 0$): the meniscus size is neglected, and the force F is an unknown of the boundary value problem.

We model such a state as a clamped-free planar beam that is subjected to a vertical end-load F. Equilibria are defined by eqs. (9) to (15) together with the end boundary conditions

$$
m_y(L/L_b) = 0\,, \ n_x(L/L_b) = 0\,, \ n_z(L/L_b) = -f \overset{\text{def}}{=} -F L_b^2/(EI) \tag{16}
$$

expressing the fact that no moment is provided by the surface and that the surface force is vertical. As seen in section 3.1, the interfacial force F on a vertical beam reaches a maximum $F_{cross} = 2\gamma w$ when the beam pierces the interface. Now if the beam is tilted (by an angle θ) the formula for the maximal force
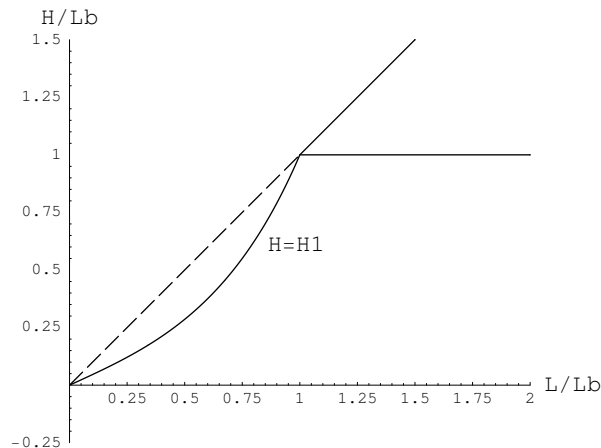

Figure 7: New version of fig.5 that includes the curve $H_1(L/L_b)$ for $L/L_b < 1$ where highly deflected states disappear.

differs. It is obtained by equating the work needed to raise a rigid beam (of width w) by a height δz with the surface energy increase due to the emersion of an area of $2w\delta l$: $F\delta z = 2\gamma w\,\delta l$ with $\delta z = \cos\theta\delta l$. Hence if a beam crosses the liquid surface (say at $s = s_1$, see fig.8), the interaction force is:

$$F_{cross} = \frac{2\gamma w}{|\cos\theta(s_1)|} \tag{17}$$

and this is also the maximal force the surface can provide to a non-piercing beam. Since a lateral displacement does not involve any change in the capillary energy, the interfacial force has no horizontal component.

In the $L > L_b$ region of the phase diagram (fig.5), the end force needed to deflect the beam never reaches F_{cross}. Conversely, when $L < L_b$, this maximal force F_{cross} defines a new boundary as we now explain. When lowering the bath height on a short ($L < L_b$) straight beam, the capillary force $2\gamma w$ is not strong enough to deflect it. The beam, partly emerged, remains straight. Now if one artificially deflects the beam and bends it into the liquid, the tangent at the end of the beam will have an angle $\theta(s_1)$ at the interface. Since the maximal capillary force that the surface can provide diverges as $|\cos\theta|^{-1}$ (eq. 17), there must be a bath height H_1 where the end force F needed to elastically bend the beam is exactly F_{cross}. For $H < H_1$ highly deflected shapes exist in addition to straight piercing shapes. This boundary, $H = H_1(L/L_b)$, is plotted in fig.7.

5.3 Piercing states

There are two types of configuration where the beam crosses the liquid surface once: 'surfacing' states where the beam crosses the surface upward and 'diving' states where the beam crosses the surface
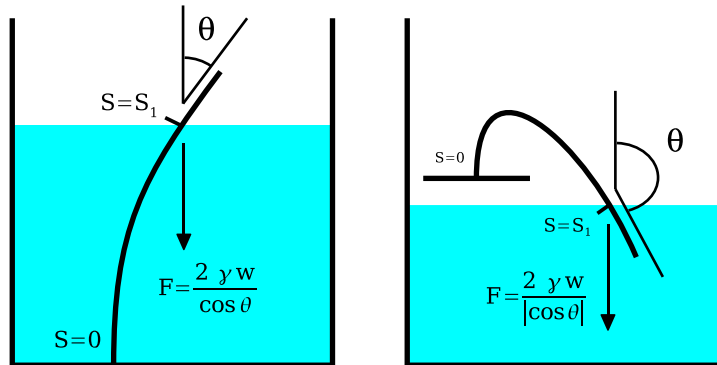
Figure 8: The two types of configuration of piercing states with $L_c = 0$. (Left) Surfacing state. These states are always unstable. (Right) Diving state. These states exist when $L/L_b > 1.2$ and $H_2 < H < 0$.

downward (see fig.8). Surfacing states were not observed experimentally because they are always unstable. Diving states (type E of fig.2) are present as soon as $L/L_b \gtrsim 1.19$.

As in the previous section, we present our model with zero capillary length. At the crossing point the interaction force between the surface and the elastic beam is $\boldsymbol{F} = -\frac{2\gamma w}{|\cos\theta|}\, \boldsymbol{e_z}$. The shape of the beam is obtained by integrating eqs. (9)-(14) in two domains: from $s = 0$ (base) to $s = s_1$ (crossing point), then from $s = s_1$ to $s = L/L_b$. At the end of the first integration we account for the surface interaction force by changing instantaneously the inner beam force vector $\boldsymbol{N}$:

$$\boldsymbol{N}(S_1^+) - \boldsymbol{N}(S_1^-) + \boldsymbol{F} = \boldsymbol{0}. \tag{18}$$

The boundary conditions at the free end are now :

$$m_y(L) = 0\,,\ n_x(L) = 0 = n_z(L). \tag{19}$$

Note that these last conditions are necessary to complete the set of equations which yields the values of the free parameters (including S_1). A precise count of free parameters and boundary conditions is given in the appendix A, section 9.

A diving state continuously turns into a twice piercing state (see section 5.5) when the bath height becomes positive. Conversely, if one lowers the bath height on a diving state, there is a critical height $H = H_2(L/L_b) \leq 0$ at which the end $s = L/L_b$ of the beam reaches the surface. Further lowering of the bath leads to an instability where the beam jumps up to a straight configuration (fig.9).

5.4 Lying states

We present here a model for the states of type C in fig.2. In such states, the beam is in interaction with the liquid along its entire length and is rigid enough to deflect the liquid surface on a large scale, comparable to its length. Indeed, part of the liquid lies above the asymptotic bath height (see fig.10). It becomes here compulsory to take the meniscus size into account.

From $s = 0$ to $s = s_1$, we integrate eqs. (9) to (14) with (15) as initial condition. At $s = s_1$, we introduce a jump in the force vector: $N(S_1^+) - N(S_1^-) + F_1 = 0$ with $F_1 = -\gamma w\, \boldsymbol{t}(s_1)$ where $\boldsymbol{t}(s)$ is the tangent vector of the beam: $\boldsymbol{t}(s) \stackrel{\text{def}}{=} x'(s)\, \boldsymbol{e_x} + z'(s)\, \boldsymbol{e_z}$. The integration between s_1 and s_2, where the
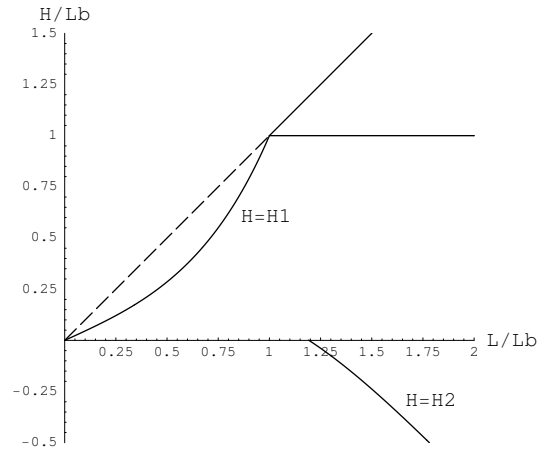
Figure 9: Extended version of fig.7 with the new curve $H = H_2(L/L_b)$ where diving states lose stability as the end of the beam detaches from the interface.
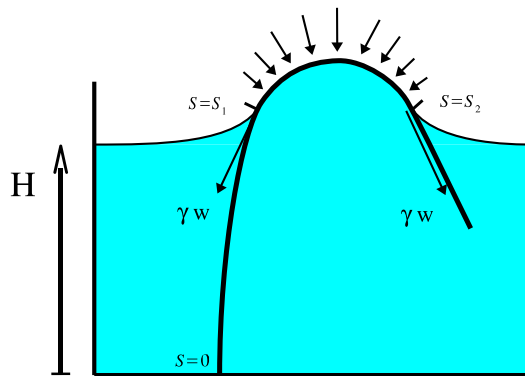

Figure 10: A lying configuration: at $s = s_1$ and $s = s_2$, the interaction with the surface is modelled by discrete jumps in the inner force vector $\boldsymbol{n}(s)$. In the region $s_1 < s < s_2$, the hydrostatic pressure yields a distributed force that is continuously changing $\boldsymbol{n}(s)$.

11

beam is *semi-submerged*, includes the hydrostatic pressure force: the liquid is raised above its asymptotic bath height, which creates a depression resulting in a distributed force $\boldsymbol{P} = \rho g w (Z - H) \boldsymbol{\nu}$ in eqs. (9) and (10), where $\boldsymbol{\nu}$ is the normal $\boldsymbol{\nu}(s) \stackrel{\text{def}}{=} \boldsymbol{t}'/|\boldsymbol{t}'| = z'(s)\boldsymbol{e_x} - x'(s)\boldsymbol{e_z}$. At $s = s_2$, we introduce another jump in the force vector : $N(S_2^+) - N(S_2^-) + F_2 = 0$ with $F_2 = +\gamma w \, \boldsymbol{t}(S_2)$. Finally, at $s = s_1$ and $s = s_2$ the meniscus is tangent to the beam, and eq.(2) requires that

$$Z(S_i) - H = L_c \sqrt{2(1 - \sin\theta(S_i))} \quad , \text{where } i = 1, 2 \, . \tag{20}$$

Note that the capillary length L_c now appears explicitly and cannot be taken as zero. Here again, we need to integrate up to the end of the beam to solve for the parameters and find s_1 and s_2.
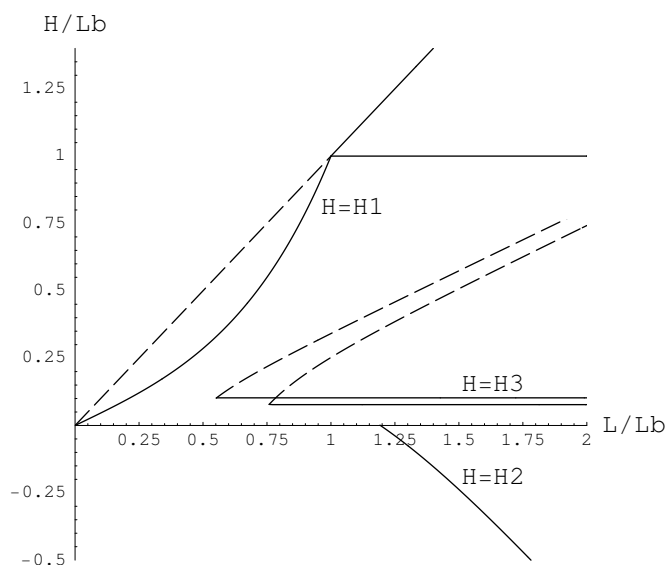

Figure 11: Extended version of figure 9 where curves corresponding to the lying state instabilities have been added. The horizontal lines ($H = H_3$) correspond to configurations where the liquid arch detaches from the beam (lower line for $L_b = 20L_c$, upper one for $L_b = 50L_c$). The oblique nearly straight curve corresponds to configurations where the end of the beam enters/exits the liquid (lower curve for $L_b = 20L_c$, upper one for $L_b = 50L_c$). The other curves (H_1, H_2, etc) are computed in the zero L_c approximation.

There are two ways for a beam to leave the lying state. First the end of the beam can reach the surface, i.e. $s_2 = L/L_b$, leading to a lightly deflected state with finite capillary length as in fig.12, right. This limit is drawn in dashed lines in fig.11 for $L_b/L_c = 20$ and 50. Computations of lightly deflected states that take the menisci into account have also been performed in order to match these lying solutions perfectly. Two types of configurations are obtained, one entirely immersed with two vertically symmetric menisci (fig.12 left), the second one having in addition a zone where the beam is semi-submerged as in a lying state (fig.12 right).

The second way for a beam to leave a lying state occurs when the transverse menisci no longer can reach the top of the arched beam. Indeed when $Z_{max} - H < 2L_c$ the overhanging liquid under the beam
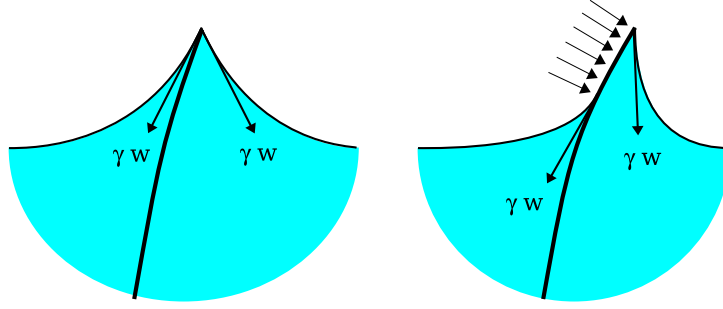
Figure 12: The two different types of configurations of lightly deflected states at non-zero L_c. Left: the two menisci joining the apex of the beam to the asymptotical bath height H are vertically symmetric. Right: the beam has a semi-submerged part.

between s_1 and s_2 is connected transversally to the surface by two menisci in the y direction. When $Z_{max} - H$ increases and crosses the limiting value $2L_c$, the liquid detaches from the beam and is replaced by air. We arrive at a twice piercing configuration (see next section). This limit H_3, which does not depend on L/L_b, is drawn in fig.11 for $L_b/L_c = 20$ and 50. Note that in the diagram of fig. 11 the others curves (H_1 and H_2) are drawn in the zero capillary length approximation and hence are not exactly coherent with this new H_3 instability line. Full coherent diagrams will be presented when comparing theory with experiments (section 6).

5.5 Twice piercing states

Along the sequence of states that are observed experimentally, the states D of fig.2 are configurations where the beam crosses the liquid surface twice. As in section 5.3, we present a model at zero capillary length. At each crossing point the interaction force between the surface and the elastic beam is $\boldsymbol{F} =$
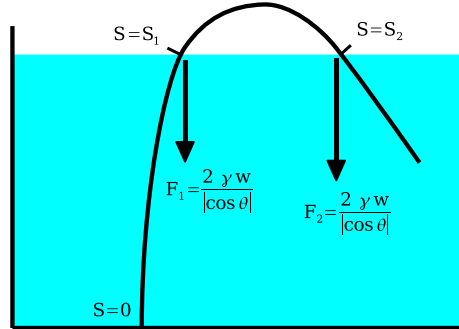

Figure 13: Twice piercing state. In the present zero capillary length approximation, left and right menisci at both crossing points (s_1 and s_2) are replaced by point forces.

$-\frac{2\gamma w}{|\cos\theta|}\,\boldsymbol{e_z}$. The shape of the beam is obtained by integrating eqs. (9)-(14) in three domains: from $s = 0$ (base) to $s = s_1$ (emersion point), then from $s = s_1$ to $s = s_2$ (immersion point), and then from $s = s_2$ to $s = L/L_b$. As before, at the end of the first integration we account for the surface interaction force by

changing instantaneously the inner beam force vector $\boldsymbol{N}$ as in eq. (18). The same is done at $s = s_2$. The boundary conditions at the free end are given by eq. (19).

Such a state has several ways in which it can disappear. First the end of the beam can reach the liquid surface: $s_2 = L/L_b$. The beam then snaps to a straight configuration, which corresponds to crossing (downward) the curve $H = H_2(L/L_b)$ with $H > 0$ in fig.14. Second a classic instability can
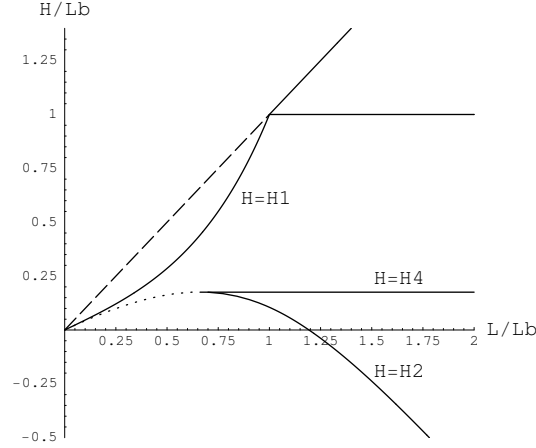

Figure 14: Extension of figure 9 where the curves corresponding to the two instabilities occurring for twice piercing states have been added (with $L_b = 50L_c$). The curve $H = H_2(L/L_b)$, corresponding to configurations where the end of the beam emerges, connects with the curve introduced for the single piercing states (see fig.9). The dotted part of the $H = H_2(L/L_b)$ curve is only plotted as a guide to the eye and does not correspond to any instability.

occur at a fold point where no configuration exists above a certain bath height. This corresponds to crossing (upward) the horizontal line H_4 in fig.14. Third, in a model at finite capillary length where left and right menisci are introduced at both crossing point ($s = s_1$ and $s = s_2$), the arch between the liquid surface and the emerged part of the beam could become so small (compared to the capillary length) that the liquid would spontaneously invade the zone and the state would change to a lying state (see section 5.4). Numerical evidence shows that this never happens for any value of L_c.

5.6 Height-deflection diagrams

Typical bifurcation diagrams, corresponding to vertical sections of the phase diagrams (e.g. fig.17) are drawn in fig.15 (for $L > L_b$) and fig.16 (for $L < L_b$). They show the different equilibrium configurations when the menisci are fully taken into account. As in our experiments the ratio L/L_b is kept fixed while the bath height is varied. When $L > L_b$ four continuous families of equilibrium configurations exist. Each family corresponds to a curve in the bifurcation diagram shown in fig.15. The vertical axis $X = 0$ consists of trivial straight states. These states are stable except in the interval $H_\beta < H < H_\alpha$, with $H_\beta = L_b - \sqrt{2}L_c$ and $L - \sqrt{2}L_c < H_\alpha < L$. From H_α (which corresponds to transition from A to B in fig. 5, where $L_c = 0$) a curve bifurcates, which includes the stable lightly deflected and lying states. This curve ends at H_3, where the overhanging liquid arch detaches. From H_β (which corresponds to transition
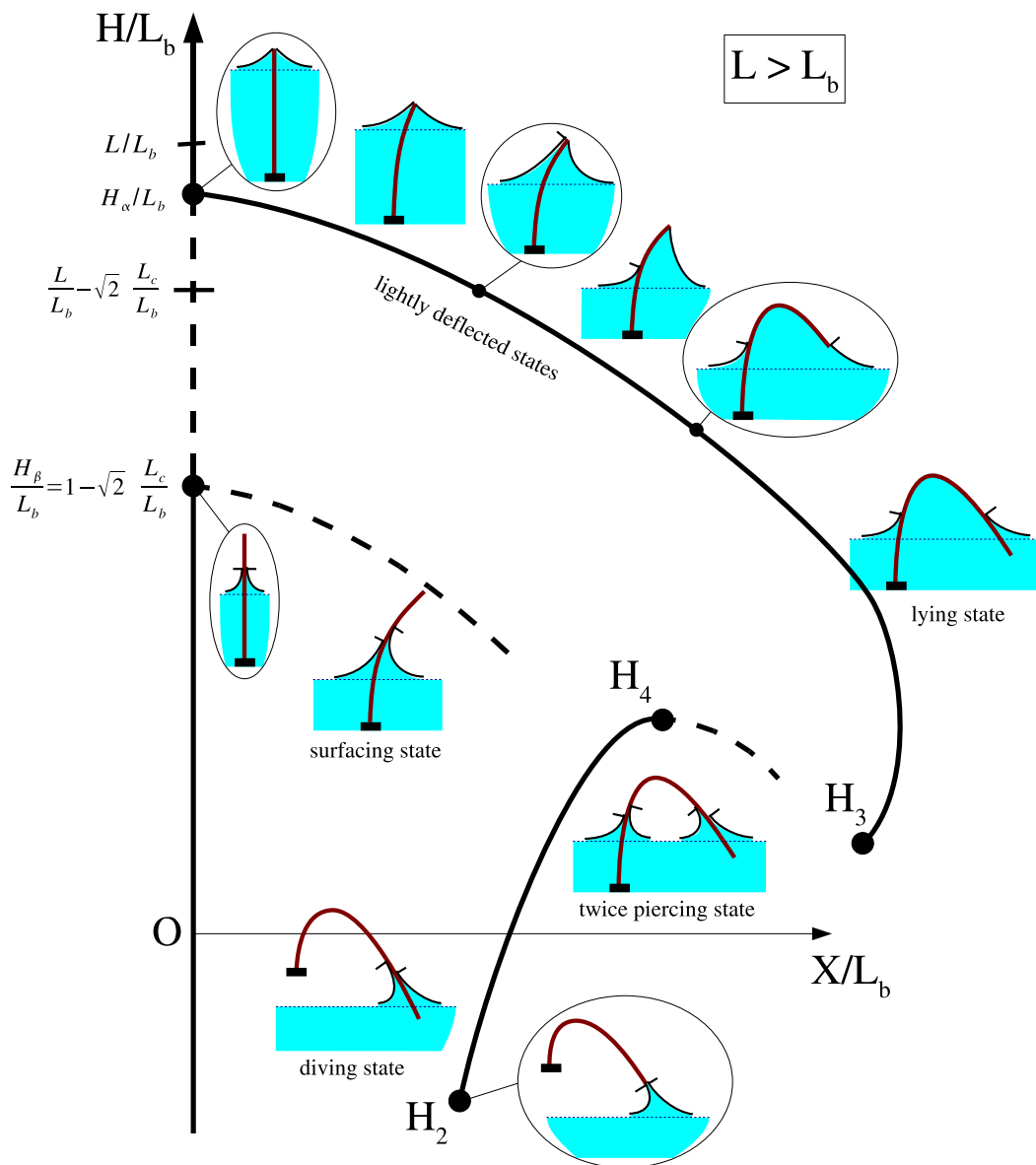
Figure 15: Typical bifurcation diagram for $L > L_b$ showing the different equilibrium configurations. The parameters X and H correspond to the lateral position of the end of the beam and to the liquid height, respectively. Plain (resp. dotted) curves corresponds to stable (resp. unstable) states.

from G to B in fig. 5, where $L_c = 0$) another curve, corresponding to unstable surfacing states, bifurcates from the trivial branch. The last curve comprises another family of stable diving states and twice piercing states. Twice piercing shapes become unstable at H_4. Note that in the interval $H_3 < H < H_4$, three different stable configurations coexist for the same bath height.

Shorter lengths, $L < L_b$, lead to a different bifurcation diagram where the trivial curve does not bifurcate; hence straight states are always stable (fig.16). Only two of the families of buckled configurations remain: stable lightly deflected and lying states, and unstable surfacing states. Studying the continuous evolution of the bifurcation diagram from fig.15 to 16 shows that the two bifurcation points H_α and H_β merge (the unstable interval of the trivial curve disappears) and lead to the intersection point H_1 of the remaining curves.
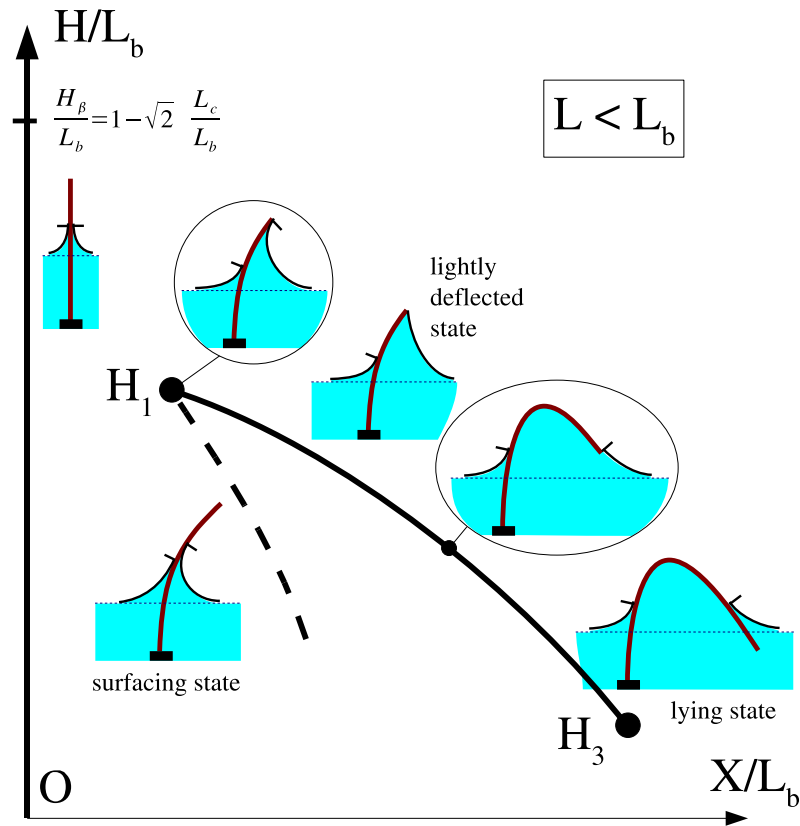

Figure 16: Typical bifurcation diagram for $L < L_b$ showing the different equilibrium configurations. The parameters X and H correspond to the lateral position of the end of the beam and to the liquid height, respectively. Plain (resp. dotted) curves corresponds to stable (resp. unstable) states.

6   Experimental results and discussion

We performed experiments using elastic strips and fibres with different bending rigidities and observed all the different equilibrium configurations described above.

16

6.1   Phase diagrams

We present in figures 17 and 18 the phase diagrams for two different strips where the transitions between possible configurations are displayed. Lengths were non-dimensionalised by the capillary buckling length L_b which was obtained by formula (6) using the measured bending rigidity. Experimental data are compared with theoretical results: the zero capillary length approximation (dotted lines), and a more comprehensive description (continuous lines), including the effects of both the weight of the strip and the menisci.
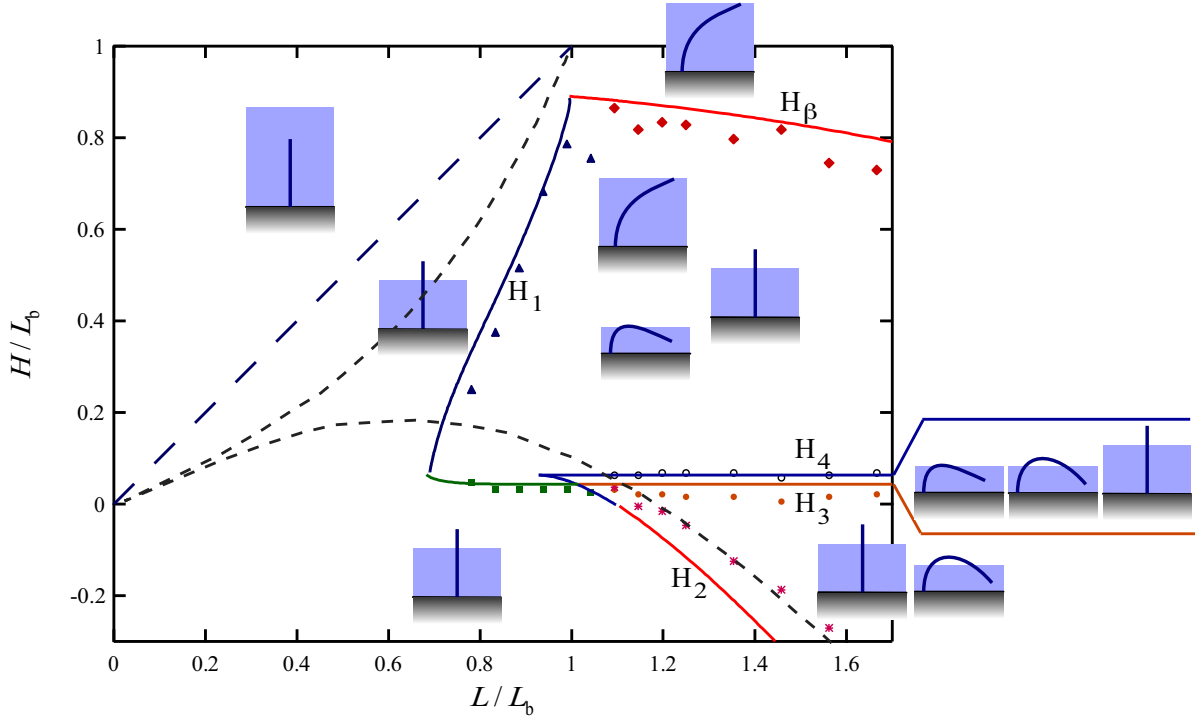

Figure 17: Experimental (symbols) and numerical (continuous lines) phase diagram for the elastic strip of thickness $e = 25\mu$m ($L_b = 1.9$ cm). In each region of the diagram the different stable configurations are sketched. The numerical computations include gravity and finite meniscus sizes, whereas dashed curves (corresponding to curves H_1 and H_2) obtained without gravity at zero capillary length ($L_c = 0$) are drawn as guides to the eye.

Let us review the transitions observed: (1) a long immersed strip buckles as it touches the surface; (2) a partially emerged straight strip buckles as the bath height H increases (plain diamonds experimental / H_β theoritical); (3) an immersed bent configuration suddenly recovers its straight shape as H is increased (triangle / H_1); (4) an immersed lying state suddenly adopts a twice piercing arch shape (full circles / H_3) or recovers its straight shape (square / H_3) as H is lowered; (5) a twice piercing arch suddenly fills up and turns into an immersed lying state (open circles / H_4) as H is increased; (6) a piercing diving arch suddenly recovers its straight shape (stars / H_2) as H is lowered. Most of these transitions are not reversible, which leads to hysteretical behaviour. Hence two (or even three) stable states coexist in many regions of the diagram.

Numerical treatment of the zero capillary length approximation reproduces qualitatively the exper-

imental transitions. However, a good quantitative agreement is achieved only once the effects of gravity and of meniscus size are included in the numerics[1]. For instance, the boundary for buckling is simply the straight line $H = L_b$, when these effects are neglected. However the height of the meniscus shifts this boundary downward. Moreover this horizontal line, once gravity is taken into account, becomes the curve H_β (see e.g. fig. 18). Indeed gravity reinforces the buckling effect, and may alone induce buckling if the beam exceeds a length $L_{bg} \sim \left(\frac{Ee^2}{\rho g} \right)^{1/3} \sim e^{2/3}$. Since the capillary buckling length L_b scales as $e^{3/2}$, thinner beams are less sensitive to gravity as confirmed by comparing fig.17 and 18. In the same way the effects of finite meniscus become important when the system length-scale tends to the capillary length: the corner defined by the intersection of dashed lines on the phase diagram is then shifted to the right, towards the intersection of the curves H_1 and H_3.
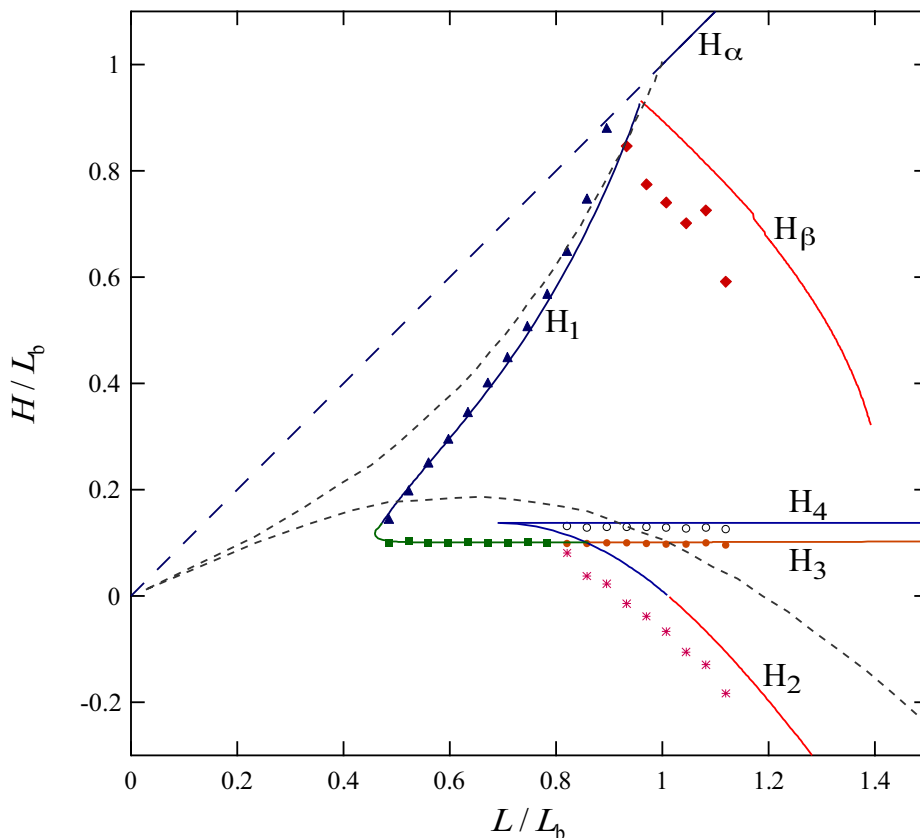

Figure 18: Experimental and numerical phase diagram for the elastic strip of thickness $e = 50\mu$m ($L_b = 6.0$ cm). Dotted curves, corresponding to curves H_1 and H_2 at zero capillary length ($L_c = 0$) are drawn as guides to the eye.

Since in practical situations, fibres are more common than strips, we conducted the same study with an elastic fibre with a circular cross section of radius $R = 18\mu$m. In this case, the buckling length L_b is obtained by replacing $2w$ by $2\pi R$ in eq. (6). We observe the same transitions as in the case of strips, see fig.19. A precise theoretical approach should include the complex computation of the three dimensional

---

[1]Gravity is represented by a term $\rho_{beam}gwe$, reduced by buoyancy into $(\rho_{beam}-\rho_{liq})gwe$ when necessary, in the distributed external force P_z in eq. (7), e being the thickness of the strip, see appendix A, section 9 for details.

shape of the meniscus around the bent rod, but we chose to present here a simplified approach. If the radius of a fibre is small compared to the capillary length, the rise of the meniscus around this vertical fibre is proportional to its radius and thus much smaller than the capillary length [14]. We therefore neglected menisci size and replaced the distributed capillary forces by concentrated ones as described in section 5 (replacing $2w$ by $2\pi R$ in eq.(17)). Conversely, it is still necessary to consider the meniscus size to describe the transition from lying to twice piercing states. In fact, in the limiting case of a horizontal rod, the shape of the meniscus is almost two-dimensional and has a maximum height that tends to $\sqrt{2}L_c$ when R becomes small compared to L_c [8]. The theoretical curves including gravity effects are drawn on fig.19 as continuous lines and they compare reasonably well with experimental data.
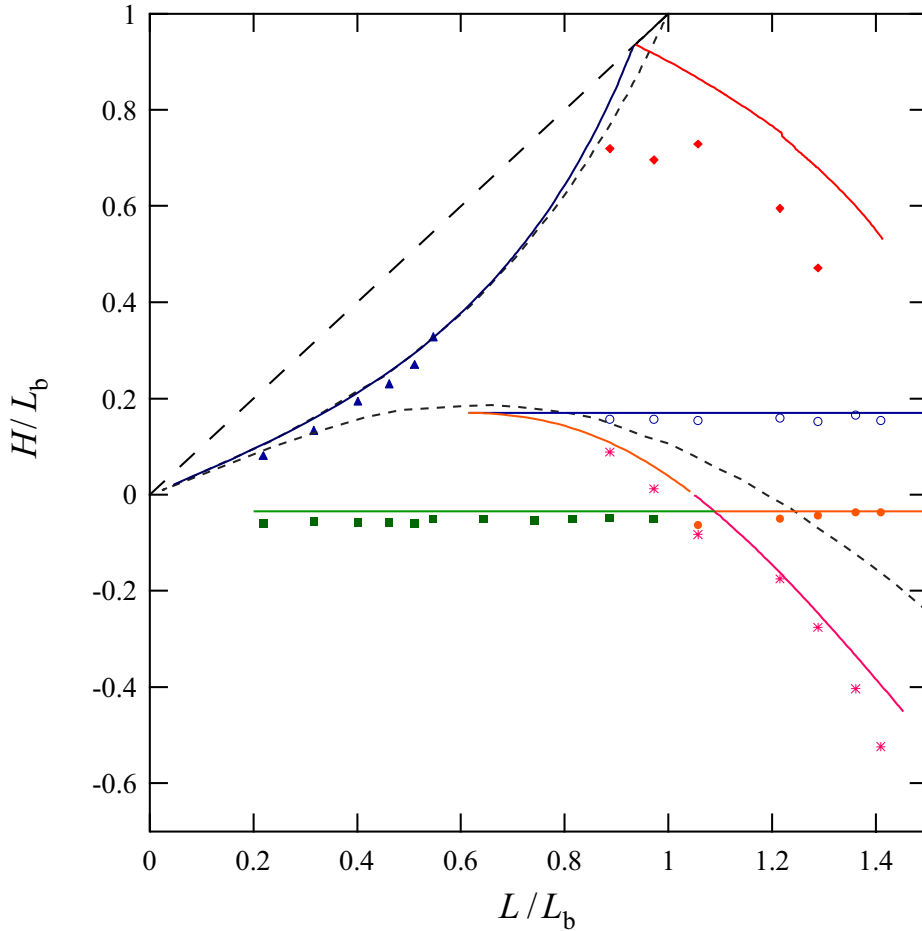

Figure 19: Experimental and numerical phase diagram for a fibre with a radius of 18 microns ($L_b = 9.8$ cm). Experimental data is plotted as symbols, whereas numerical curves are in continuous line (with gravity) or dotted lines (without gravity).

6.2 Shapes

In addition to the phase diagram, the model also yields the different equilibrium shapes. Interestingly, some shapes can be deduced one from another using two geometrical constructions.
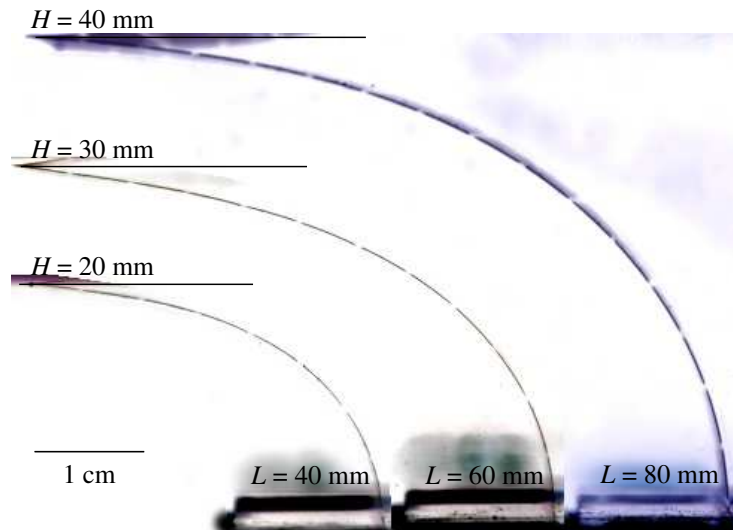
Figure 20: For the same ratio H/L, lightly deflected shapes are homothetic.

For lightly deflected states considered at zero capillary length, the liquid surface acts as a frictionless rigid wall. These states only depend on the length of the strip and the bath height. As a result they are self-similar and are characterised by the dimensionless ratio L/H. The bent shapes corresponding to points on a line of the phase diagram passing through the origin with a slope L/H are homothetic to the same master shape, as confirmed by experiments (fig.20).

Conversely in the double piercing states and lying states the terminal portion of the strip is completely immersed in the liquid and thus free from any force or torque (if gravity is ignored). This last portion stays straight and can be lengthened arbitrarily without any change in the other part of the strip, as can be verified in the experiments (fig.21). This construction provides a new shape with the same H, but a larger L, *i.e.* along a horizontal line on the phase diagram.

7   Conclusion

The simple question of whether or not an elastic rod can pierce a liquid interface has led us to a rich set of equilibrium configurations. The observed behaviour depends on two key length-scales, the elasto-capillary length L_{EC} which gives the typical radius of curvature produced by capillary forces on an elastic slender body, and the capillary length L_c which compares gravity and surface tension and gives the typical size of a liquid meniscus. In particular, we found a critical length L_b proportional to L_{EC} above which a rod cannot pierce a liquid interface but buckles. The postbuckling evolution of the system is complex, involves strong hysteresis and the coexistence of up to three stable concurrent configurations. We explored in details these different configurations and their stability. Experimental results are found in close agreement with numerical computations of equilibria of Kirchhoff elastic rods submitted to capillarity, hydrostatics, and gravity.

We believe these results can be useful to the design of micro-electro-mechanical systems and nano-structures in wet environment [19, 17, 13], or to understand the locomotion of insects on water [12], since capillary deflections of elastic structures are enhanced at small scales.
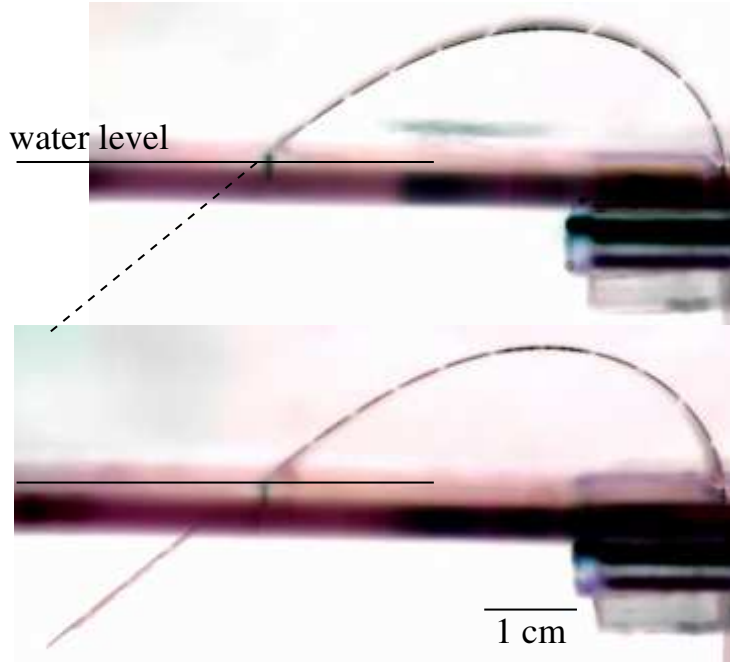
Figure 21: Free end configurations may always be lengthen without change. These two configurations with the same bath height have different lengths but an identical emerged part.

8 Acknowledgements

9 Appendix A

We give here a detailed presentation of our numerical scheme involving a meniscus for one example of configuration: a diving beam (see fig.22).

The values of L, L_b, L_c are fixed. In this approach H is not a parameter but is calculated *a posteriori*. The initial conditions at the clamped end ($s = 0$) are:

$$x(0) = 0 = z(0) \,, \theta(0) = 0. \tag{21}$$

The values of normalised forces and torques $n_x(0)$, $n_z(0)$, $m_y(0)$ are unknowns of the boundary value problem. The differential equations are eqs.(9)-(14) where p_x and p_z take different forms depending on the part of the beam under consideration. From $s = 0$ to $s = s_1$, the weight is the only distributed external force that acts on the beam:

$$p_x \equiv 0 \ \text{ and } \ p_z = \frac{1}{2} \left(\frac{\pi}{2}\right)^2 \frac{\rho_{beam}}{\rho_{liq}} \frac{eL_b}{L_c^2} \,. \tag{22}$$
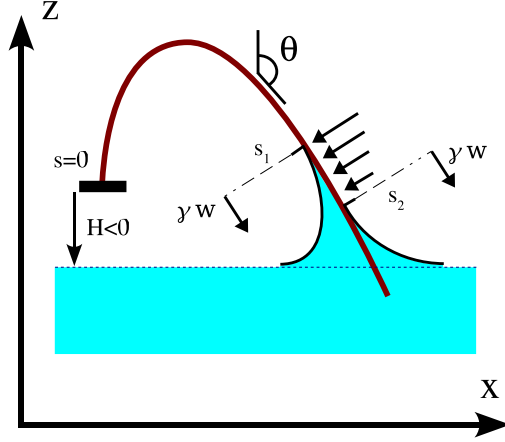
Figure 22: A diving beam, piercing the surface once.

At $s = s_1$ a discrete jump in the force vector due to capillarity is introduced. This point force is tangent to the beam:

$$n_x(s_1^+) - n_x(s_1^-) = -\frac{1}{2}\left(\frac{\pi}{2}\right)^2 \sin\theta(s_1) < 0 \tag{23}$$

$$n_z(s_1^+) - n_z(s_1^-) = -\frac{1}{2}\left(\frac{\pi}{2}\right)^2 \cos\theta(s_1) > 0. \tag{24}$$

From s_1 to s_2, the beam undergoes a pressure difference between air on one side and a depressed liquid on the other side. This pressure force is added to the weight of the beam:

$$p_x = -\frac{1}{2}\left(\frac{\pi}{2}\right)^2 \left(\frac{L_b}{L_c}\right)^2 [z(s) - h]\cos\theta(s), \tag{25}$$

$$p_z = +\frac{1}{2}\left(\frac{\pi}{2}\right)^2 \left(\frac{L_b}{L_c}\right)^2 [z(s) - h]\sin\theta(s) + \frac{1}{2}\left(\frac{\pi}{2}\right)^2 \frac{\rho_{beam}}{\rho_{liq}} \frac{eL_b}{L_c^2}. \tag{26}$$

For $s = s_2$ a second discrete jump in the force vector is added in the same way as in s_1. Finally from $s = s_2$ to the end of the beam $s = L/L_b$, the weight of the beam is reduced by the buoyancy effect:

$$p_x \equiv 0 \quad \text{and} \quad p_z = \frac{1}{2}\left(\frac{\pi}{2}\right)^2 \frac{\rho_{beam} - \rho_{liq}}{\rho_{liq}} \frac{eL_b}{L_c^2}. \tag{27}$$

The final boundary conditions at the end of the beam $s = L/L_b$ are that no force and no moment are provided to the beam (free end conditions): $n_x(L/L_b) = 0$, $n_z(L/L_b) = 0$, $m_y(L/L_b) = 0$.

The arclengths s_1 and s_2 are not fixed *a priori*. The shape of the two menisci is such that the height of menisci i at s_i is given by $z(s_i) - h = \sqrt{2}\,(L_c/L_b)\sqrt{1 - \sin\theta(s_i)}$. This implies a further condition:

$$z(s_1) - z(s_2) = \sqrt{2}\,(L_c/L_b)\left(\sqrt{1 - \sin\theta(s_1)} - \sqrt{1 - \sin\theta(s_2)}\right). \tag{28}$$

The complete boundary value problem has then five unknowns $n_x(0)$, $n_z(0)$, $m_y(0)$, s_1, s_2 and four conditions given by eqs.(21) and (28). Hence for each type of configuration, the solution manifold of

the problem is a discrete set of one dimensional curves in the five dimensional space. We compute these curves using a continuation algorithm based on multiple shooting techniques.

A final remark: in the model at zero capillary length, a concentrated force is invoked each time the beam crosses the liquid surface, eq.(17). In the finite capillary length model, the crossing region extends from s_1 to s_2. If the elastic beam were straight in this region the total force applied on the beam (i.e. the two jumps at s_1 and s_2, and the pressure difference) would be exactly given by eq. (17).

10 Appendix B

We show here that all equilibrium solutions of piercing or capillary deflected beams are planar. This property is due to the end boundary condition where no moment is applied, and to the fact that capillary and pressure forces are in the local osculating plane of the tangent and normal vectors. In the general three dimensional twisted case, an equilibrium state of a Kirchhoff rod must satisfy eqs. (7) and (8) together with linear constitutive equations [1]. We here restrict ourselves to the case where the rod is unshearable, inextensible and has an isotropic cross-section and material, but we conjecture that the present proof can be generalised to more general rods. It has been shown that in the isotropic case the full set of equilibrium equations can be reduced [18] to:

$$\boldsymbol{N}' + \boldsymbol{P} = \boldsymbol{0}\,, \quad \boldsymbol{M}' = \boldsymbol{N} \times \boldsymbol{t}\,, \quad \boldsymbol{t}' = \boldsymbol{M}' \times \boldsymbol{t}\,, \tag{29}$$

where $\boldsymbol{t} = \boldsymbol{R}'$ is the tangent to the centre line $\boldsymbol{R}$, and $\boldsymbol{N}$ and $\boldsymbol{M}$ are the internal force and moment and $\boldsymbol{P}$ is an external force. We first establish an important property about the solutions of (29).

Property 10.1. *If at a point $S = S_1$, $t_y(S_1) = 0$, $N_y(S_1) = 0$, $M_x(S_1) = 0$, $M_z(S_1) = 0$, and $P(S_1) = 0$ and $\forall S \in [S_1; S_2]$, $P_y(S) = 0$, then in the interval $S \in [S_1; S_2]$, the solutions of (29) are such that $t_y(S) \equiv 0$, $N_y(S) \equiv 0$, $M_x(S) \equiv 0$, $M_z(S) \equiv 0$.*

Proof. Since $P_y \equiv 0$ for $S \in [S_1; S_2]$ then $N_y(S) = N_y(S_1) + \int_{S_1}^{S_2} P_y(S)dS \equiv 0$. The equations (29) implies in particular that:

$$t'_y = M_z\, t_x - M_x\, t_z \tag{30}$$
$$M'_x = -N_z\, t_y \tag{31}$$
$$M'_z = N_x\, t_y \tag{32}$$

and we directly see that the manifold $(t_y, M_x, M_z) = (0, 0, 0)$ is an invariant manifold under the S evolution. Since we start on it at S_1, we stay on it up to S_2. We hence have $\forall S \in [S_1; S_2]$, $t_y(S) \equiv 0$, $M_x(S) \equiv 0$, $M_z(S) \equiv 0$. $\qquad\square$

We consider a (possibly 3D) equilibrium solution satisfying the following boundary conditions: the rod is clamped at its base ($S = 0$) and its end ($S = L$) is either standing in the air (surfacing state), deflecting the liquid surface (lightly deflected state), or immersed (e.g. lying state). In any case, and this is the important point here, no moment is applied at the end. The rod is subjected to gravity and we call z the vertical axis. Without loss of generality we choose the x and y axis such that the tangent at $S = L$ is in the (x, z) plane, that is $t_y(L) = 0$. At this point the internal force $\boldsymbol{N}$ and external force $\boldsymbol{P}$ (e.g. gravity, buoyancy, or capillarity) have the property that $N_y(L) = 0 = P_y(L)$. The internal moment is zero, so in particular we have $M_x(L) = 0 = M_z(L)$. In between the point $S = L$ and the first surface crossing point $S = S_2$, the external forces (gravity and/or buoyancy only) have the property that for

$S \in [S_2; L]$, $P_y(S) \equiv 0$. We see that the hypotheses of property 10.1 (with $L = S_1$) are fulfilled and we can infer that until $S = S_2$ we have $t_y(S) \equiv 0$, $N_y(S) \equiv 0$, $M_x(S) \equiv 0$, $M_z(S) \equiv 0$: the internal moment only has a bending component M_y, the rod lies in the plane (x, z), and so does the internal force.

At the crossing point S_2, where the rod tangent is in the (x, z) plane, the external capillary forces have the property that $P_y(S_2) = 0$. Consequently the same argument can be held to show that up to the next surface crossing point $S = S_3$, the rod lies in the plane (x, z), with its internal force in the plane and its internal moment orthogonal to it. This argument can be carried up to the clamped base.

In conclusion, we have shown that a rod subjected to capillary, gravity and buoyancy forces without any applied moment at its end has only planar equilibria.

References

[1] S. S. Antman. *Nonlinear problems of elasticity*. Springer-Verlag, New York, 2nd edition, 2004.

[2] José Bico, Arezki Boudaoud, and Benoît Roman. Elastocapillary coalescence in wet hair. *Nature*, 432:690, December 2004.

[3] N. Chakrapani, B. Wei, A. Carrillo, P. M. Ajayan, and R. S. Kane. Capillarity-driven assembly of two-dimensional cellular carbon nanotube foams. *Proc. Natl Acad. Sci. USA*, 101:4009–4012, 2004.

[4] Christophe Clanet and David Quéré. Onset of menisci. *Journal of Fluid Mechanics*, 460:131–149, 2002.

[5] Adam E. Cohen and L. Mahadevan. Kinks, rings, and rackets in filamentous structures. *Proceedings of the National Academy of Sciences, USA*, 100(21):12141–12146, 2003.

[6] Pierre-Gilles de Gennes. Wetting: statics and dynamics. *Review of Modern Physics*, 57:827–863, 1985.

[7] Pierre-Gilles de Gennes, Francoise Brochard-Wyard, and David Quere. *Capillarity and Wetting Phenomena: Drops, Bubbles, Pearls, Waves*. Springer-Verlag New York, 2003.

[8] B.B. Freud and H.Z. Freud. A general theory for calculating surface tension from the shapes of stable liquid surfaces of revolution. *Science*, 72(1869):435–436, 1930.

[9] A. K. Geim, S. V. Dubonos, I. V. Grigorieva, K. S. Novoselov, A. A. Zhukov, and S. YU. Shapoval. Microfabricated adhesive mimicking gecko foot-hair. *Nature Materials*, 2(7):461–463, 2003.

[10] D. Halpern and J.B. Grotberg. Fluid-elastic instabilities of liquid-lined flexible tubes. *Journal of Fluid Mechanics*, 244:615–632, 1992.

[11] A. L. Hazel and M. Heil. Surface-tension-induced buckling of liquid-lined elastic tubes – a model for pulmonary airway closure. *Proceedings of the Royal Society A*, 461:1847–1868, 2005.

[12] D.L. Hu and J.W.M. Bush. Meniscus-climbing insects. *Nature*, 437:733–736, 2005.

[13] C. Y. Hui, A. Jagota, Y. Y. Lin, and E. J. Kramer. Constraints on microcontact printing imposed by stamp deformation. *Langmuir*, 18:1394–1407, 2002.

[14] D. F. James. The meniscus on the outside of a small circular cylinder. *J. Fluid Mechanics*, 63:657–664, 1974.

[15] Joseph B. Keller. Surface tension force on a partly submerged body. *Physics Fluids*, 10(11):3009–3010, 1998.

[16] Kenneth K. S. Lau, José Bico, Kenneth B. K. Teo, Manish Chhowalla, Gehan A. J. Amaratunga, William I. Milne, Gareth H. McKinley, and Karen K. Gleason. Superhydrophobic carbon nanotube forests. *Nano Letters*, 3(12):1701–1705, 2003.

[17] C. H. Mastrangelo and C. H. Hsu. Mechanical stability and adhesion of microstructures under capillary forces. *J. Microelectromech. Syst.*, 2:33–55, 1993.

[18] Sébastien Neukirch and Michael E. Henderson. Classification of the spatial clamped elastica: symmetries and zoology of solutions. *Journal of Elasticity*, 68:95–121, 2002.

[19] O. Raccurt, F. Tardif, F.A. d'Avitaya, and T. Vareine. Influence of liquid surface tension on stiction of SOI MEMS. *Journal of Micromechanics and Microengineering*, 14(7):1083–1090, 2004.

[20] Pere Roca-Cusachs, Felix Rico, Elena Martinez, Jordi Toset, Ramon Farré, and Daniel Navajas. Stability of microfabricated high aspect ratio structures in poly(dimethylsiloxane). *Langmuir*, 21:5542–5548, 2005.

[21] T. Tanaka, M. Morigami, and N. Atoda. Mechanism of resist pattern collapse during development process. *Japanese Journal of Applied Physics*, 32:6059–6064, 1993.

[22] Stephen P. Timoshenko and James M. Gere. *Theory of Elastic Stability*. McGraw-Hill international editions, 1961.